Competing mechanisms determine oxygen redox in doped Ni-Mn based layered oxides for Na-ion batteries

Yongchun Li,[1] Katherine A. Mazzio,[1,2,*] Najma Yaqoob,[3,5] Yanan Sun,[1,2] Annica I. Freytag,[1,2] Deniz Wong,[2] Christian Schulz,[2] Volodymyr Baran,[4] Alba San Jose Mendez,[4] Götz Schuck,[2] Marcin Zając,[6] Payam Kaghazchi,[3,5] and Philipp Adelhelm[1,2,*]

1 Humboldt-University Berlin, Brook-Taylor-Str. 2, 12489 Berlin, Germany

2 Helmholtz-Zentrum Berlin für Materialien und Energie, GmbH, Hahn-Meitner-Platz 1, 14109 Berlin Germany

3 Forschungszentrum Jülich GmbH, Institute of Energy and Climate Research Materials Synthesis and Processing (IEK-1) 52425 Jülich, Germany

4 Deutsches Elektronen-Synchrotron (DESY), Notkestraße 85, 22607 Hamburg, Germany

5 MESA+ Institute for Nanotechnology, University of Twente, 7500 AE Enschede, the Netherlands

6 National Synchrotron Radiation Centre SOLARIS, Czerwone Maki 98, 30-392 Kraków, Poland

E-mail: katherine.mazzio@hu-berlin.de, philipp.adelhelm@hu-berlin.de

Keywords: Na-ion batteries, layered oxides, Mg doping, Sc doping, oxygen redox, anion redox, RIXS

Abstract

Cation doping is an effective strategy for improving the cyclability of layered oxide cathode materials through suppression of phase transitions in the high voltage region (above ~4.0 V). However, different dopants have been shown to have different impacts on the potential profiles in these regions, such as inducing more sloping behavior or truncating the high voltage plateau, thereby indicating that more than one dopant-dependent mechanism is at play in these materials. In this study we choose Mg and Sc as representative dopants in P2-$Na_{0.67}Ni_{0.33}Mn_{0.67}O_2$. While both dopants have a positive effect on the cycling stability, they are found to influence the properties in the high voltage regime in different ways. Through a combination of RIXS, XRD, XAS, PDF analysis, and DFT, we show that it is more than just

suppression of the P2 to O2 phase transition that is critical for promoting the favorable properties, and that the interplay between Ni and O activity are also critical aspects that dictate the performance. In the case of Mg doping, we found that we could enhance the Ni activity while simultaneously suppressing the O activity. This is surprising because it is in contrast to what has been reported in other Mn-based layered oxides where Mg is known to trigger oxygen redox. We address this contradiction by proposing a competing mechanism between Ni and Mg that impacts differences in O activity in $Na_{0.67}Mg_xNi_{0.33-x}Mn_{0.67}O_2$ (x<0<0.33). These findings provide a new direction in understanding the effects of cation doping on the electrochemical behavior of layered oxide materials.

Introduction

Sodium-ion batteries (SIBs) are gaining importance as promising alternatives to lithium-ion batteries (LIBs) for grid and large-scale energy storage applications due to the high Earth abundance of the elements used in SIBs such as Na, Fe, and Mn.[1] However, the energy density urgently needs further improvement to meet increasing energy storage demands.[1b] Stable and high-capacity positive electrodes are a prerequisite for increasing the energy density of SIBs. Among the various reported cathode materials, layered oxides are ideal candidates because they can have tunable compositions with reasonable capacity and the electrochemical performance can be easily tailored by introducing different elements into the host structures.

Ni-Mn based layered cathode materials have attracted much attention in both LIBs and SIBs due to the high operating voltage of the Ni redox and its multiple electron couples ($Ni^{2+} \rightarrow Ni^{3+} \rightarrow Ni^{4+}$). In these materials, Ni is not only an active element that provides capacity, but it can also trigger oxygen redox when the voltage is above 4.1 V. This has been found for a variety of different Ni/Mn ratios, e.g. compositions of $Na_{0.78}Ni_{0.23}Mn_{0.69}O_2$, $Na_{0.67}Ni_{0.2}Mn_{0.8}O_2$, $Na_{0.5}Ni_{0.25}Mn_{0.75}O_2$, and $Na_{0.67}Ni_{0.33}Mn_{0.67}O_2$.[2] Among these materials, $Na_{0.67}Ni_{0.33}Mn_{0.67}O_2$ is one of the most common compositions, and it is known to have a P2 phase in SIBs (following Delmas' notation).[3] Although oxygen redox in the high voltage region is known to initially improve the storage capacity in layered oxides, it ultimately can result in capacity fade due to a combination of oxygen loss and cation migration.[4] Another process that causes capacity

fade is the phase transition from P2 to O2 which leads to significant volume changes and has been reported to start when exceeding approximately 4.1 V.[5] Therefore, finding a balance between stability and high capacity is required for future battery applications.

Cation doping, or more specifically ion substitution, is an effective and practical strategy for achieving superior properties in cathode materials, which has been widely demonstrated in both laboratory experiments and commercial products. With respect to P2-$Na_{0.67}Ni_{0.33}Mn_{0.67}O_2$, the use of Li^+, Mg^{2+}, Cu^{2+}, and Zn^{2+} as substitutional elements has been found to be effective for tailoring the material properties.[5a, 6] Suppression of the P2 to O2 phase transition is considered to be the most important reason for the better electrochemical properties by doping with these cations. In these systems, instead of a flat voltage plateau, a sloping potential profile can be observed for voltages above 4.0 V. This behavior has also been found in many systems where Ni and Li^+ coexist with Mg^{2+}, Cu^{2+}, or Zn^{2+}.[7] The origins of the sloping electrochemical behavior are still unknown, but they may be a result of a solid-solution type storage mechanism, kinetic effects, or different electrochemical contributions, among others. Similarly, the relationship between the sloping potential profiles and the P2 to O2 phase transition have not yet been well described, making further investigations necessary.

In this work we study the impact of doping with Mg and Sc on P2-$Na_{0.67}Ni_{0.33}Mn_{0.67}O_2$. Through a combination of resonant inelastic X-ray scattering (RIXS), *operando* X-Ray diffraction, X-ray absorption spectroscopy (XAS), X-ray pair distribution function analysis (PDF), and density functional theory (DFT), we found that while Mg and Sc can both decrease the oxygen activity through reduction of the Ni content, they have very different structural responses during cycling. Where the undoped (largest volume change) and Mg-doped samples (intermediate volume change) exhibit structural reversibility, the Sc-doped sample (lowest volume change) shows irreversible structural changes. These results were surprising at first because they point towards redox behavior being more critical than structural changes for improved cycle life in these materials. To further understand the role of Mg in suppressing the oxygen redox activity, we varied the amount of Mg doping and found that there exists a competition between Ni and Mg for triggering oxygen redox in $Na_{0.67}Mg_xNi_{0.33-x}Mn_{0.67}O_2$ which is therefore dependent on the molar ratio of Mg/Ni.

Results

Undoped and Mg-, Sc-doped (10%) samples:

The crystal structures of $Na_{0.67}Ni_{0.33}Mn_{0.67}O_2$ (designated as P2-NaNMO), $Na_{0.67}Mg_{0.1}Ni_{0.23}Mn_{0.67}O_2$ (designated as P2-NaM$_{0.10}$NMO), and $Na_{0.67}Sc_{0.1}Ni_{0.23}Mn_{0.67}O_2$ (designated as P2-NaS$_{0.10}$NMO) were analyzed by powder X-ray diffraction (XRD) and Rietveld refinement. Each material was found to have a layered structure with space group $P6_3/mmc$ without any impurities (see Figure S1, Table S1-S3). The sodium storage performance of the three cathode materials was evaluated at a current density of 20 mA g^{-1} in a voltage range of 2.5-4.4 V, as shown in Figure 1. Due to a higher Ni content in the undoped material (P2-NaNMO), the charge/discharge capacities of P2-NaNMO are 150/136 mAh g^{-1}, which is higher than that of P2-NaM$_{0.10}$NMO (128/118 mAh g^{-1}) and P2-NaS$_{0.10}$NMO (136/122 mAh g^{-1}). Compared to the undoped material, the Mg and Sc doped materials exhibit much smoother charge/discharge curves below 4.0 V. In the high voltage region up to 4.4 V, significant differences between different materials were observed. There is a long and flat high voltage plateau for the P2-NaNMO sample, which can deliver a capacity of about 70 mAh g^{-1} (out of 150 mAh g^{-1} for the full charge capacity in the 1st cycle). P2-NaS$_{0.10}$NMO has a similar high voltage plateau, but it is shorter than that of the undoped P2-NaNMO, and only delivers a capacity of about 45 mAh g^{-1} (out of 136 mAh g^{-1} for the full charge capacity in the 1st cycle). In contrast, the Mg-doped material shows a sloping potential profile in the high voltage region, and the corresponding dQ/dV curve shows the lowest signal intensity above 4.0 V among the investigated materials, indicating that Mg doping suppresses the high voltage plateau more completely. The Sc-doped material shows electrochemical behavior similar to that of the undoped P2-NaNMO material, which also shows a high intensity peak above 4.0 V in the dQ/dV curve. These observations demonstrate that the two dopants have different roles in the electrochemical reaction. During long-term cycling, it can be seen that P2-NaM$_{0.10}$NMO shows the best stability, delivering a reversible capacity of 58 mAh g^{-1} after 500 cycles and 160 days. Under the same conditions, P2-NaS$_{0.10}$NMO and undoped P2-NaNMO only deliver capacities of 38 and 3 mAh g^{-1}, respectively (see Figure 1d, e and Figure S3). Based on the excellent Na storage of P2-NaM$_{0.10}$NMO, it can be concluded that suppressing the high voltage plateau is a promising strategy for enhancing the properties of P2-$Na_{0.67}Ni_{0.33}Mn_{0.67}O_2$.

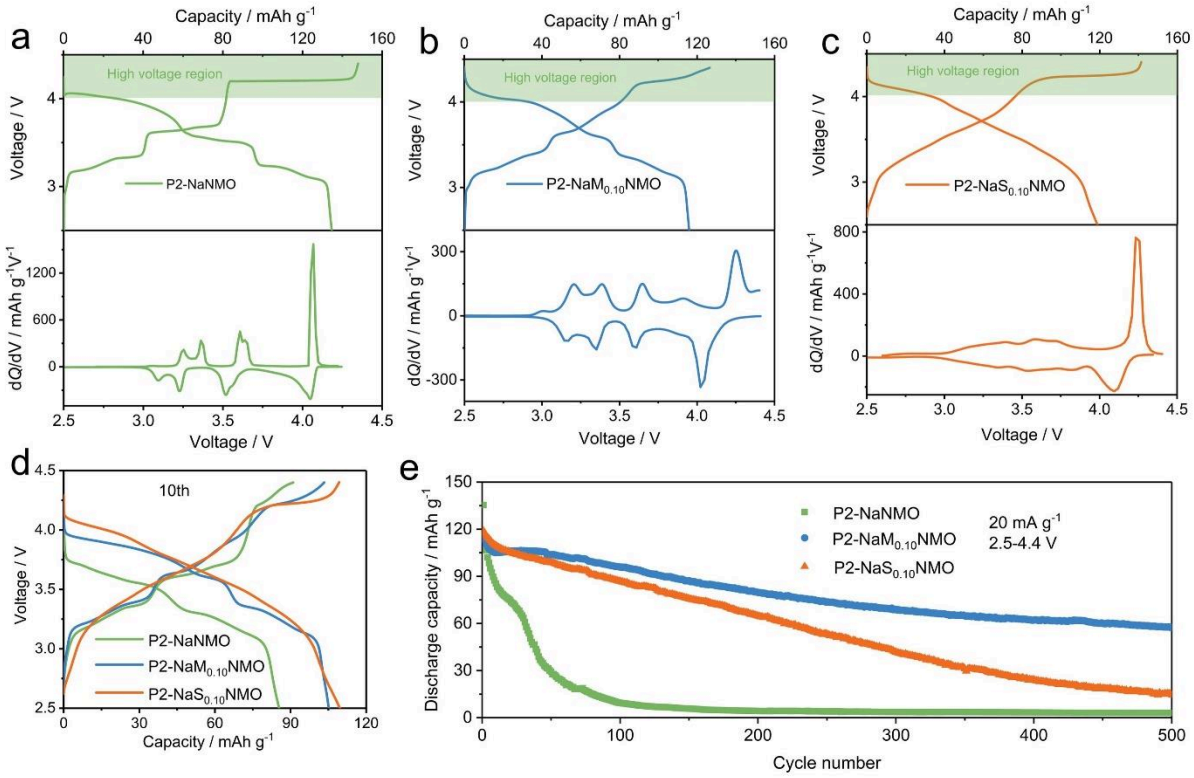

Figure 1 Electrochemical properties at a current density of 20 mA g^{-1} (0.1 C) in the voltage range of 2.5-4.4 V. (a-c) First charge/discharge profiles and corresponding d*Q*/dV curves for P2-NaNMO, P2-$NaM_{0.10}$NMO, and P2-$NaS_{0.10}$NMO, respectively. (d) Charge/discharge curves at the 10th cycle. (e) Discharge capacity over 500 cycles.

Oxygen redox can be triggered at high voltages, which has been shown for many layered oxides above 4.0 V.[8] Here, we used Resonant Inelastic X-ray Scattering (RIXS) to identify differences in the oxygen redox behavior for the different compositions. Figure 2 (a-c) shows the results of RIXS measurements at the O *K*-edge for P2-NaNMO, P2-$NaM_{0.10}$NMO, and P2-$NaS_{0.10}$NMO at open-circuit voltage (OCV), when fully charged to 4.4 V, and when fully discharged to 2.5 V during the first cycle. The spectra for the OCV and the fully discharged state were similar for all samples. However, at the fully charged state, a new energy loss peak at 8 eV can be observed, which is consistent with the associated oxygen redox signal reported by Bruce et al. and Yang et al.[9] The intensity of this peak is different among the three samples, with the highest intensity observed for P2-NaNMO followed by P2-$NaS_{0.10}$NMO and P2-$NaM_{0.10}$NMO. Figure 2d highlights the region near 0 eV of the RIXS spectra of the three states for each material. A progression of sharp peaks can be observed only in the fully charged state, which are associated with vibrations arising from molecular O_2 units. The distance between

the first peak and 0 eV can be used to identify the oxygen species, where an energy of 0.194 eV was first reported as molecular O_2 by Bruce et al.[9] These molecular O_2 units are not necessarily released from the host structure, but exist as trapped dimers within the crystal structure at the charged state.[4a, 9a, 9b] Among the three materials, the intensity of the vibration signals for molecular O_2 in the P2-Na$M_{0.10}$NMO material are the lowest and exhibit the fastest attenuation within the energy loss window. This is consistent with a lower intensity of the oxygen redox signal at an energy loss of 8 eV. The findings confirm that oxygen redox occurs for all samples at varying degrees and that the Mg-doped shows the smallest oxygen redox activity. The related mechanism is discussed in more detail below.

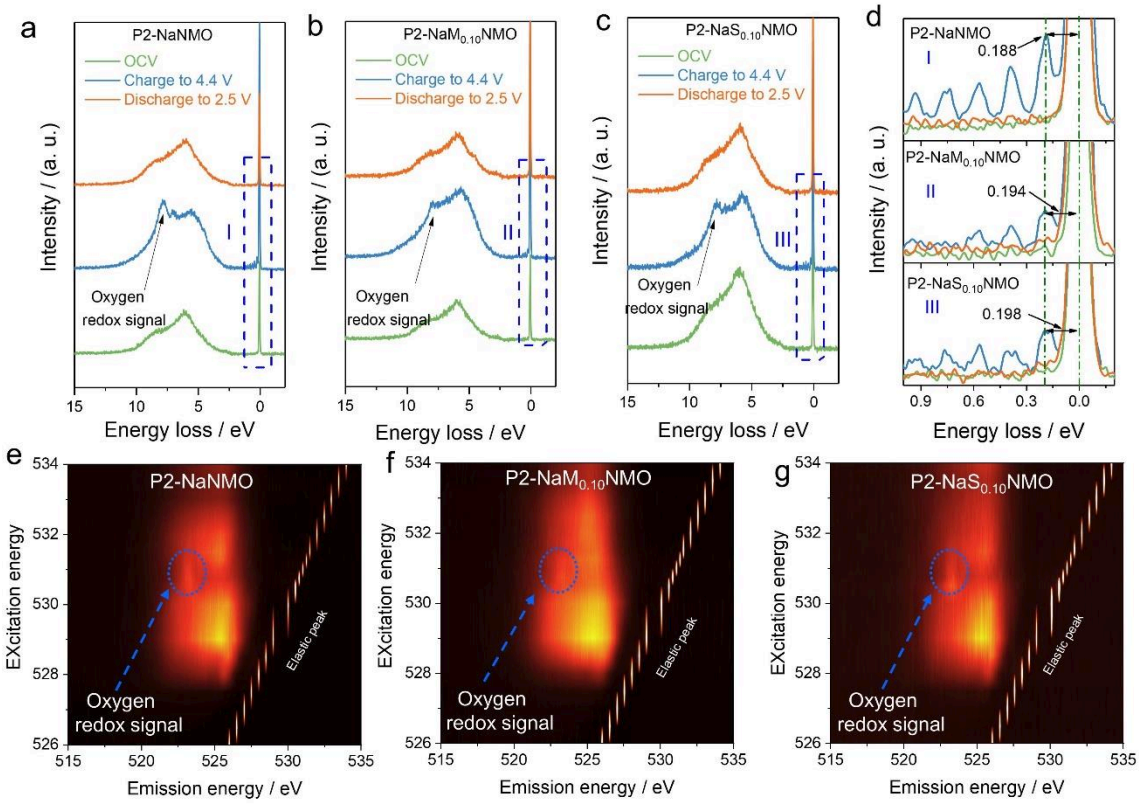

Figure 2 (a-c) O *K*-edge RIXS spectra with an excitation energy of 531 eV for P2-NaNMO, P2-Na$M_{0.10}$NMO, and P2-Na$S_{0.10}$NMO at OCV, charged to 4.4 V, and discharged to 2.5 V states. (d) Magnified RIXS spectra for each sample (I, II, III) in the three states. O *K*-edge RIXS maps with excitation energy ranging from 526 to 534 eV of (e) P2-NaNMO, (f) P2-Na$M_{0.10}$NMO, and (g) P2-Na$S_{0.10}$NMO at 4.4 V.

In order to more clearly observe differences in the oxygen redox of the three samples, RIXS mapping was conducted on samples in the fully charged state with an excitation energy between 526 and 534 eV. The results are presented in Figure 2(e-g), where it can be seen that

there is a significant difference at the excitation energy between 530.5 and 531.5 eV (marked by blue dotted circles), which is where the features associated with the oxygen redox arise.[2d, 9-10] The undoped material and Sc-doped material both show a bright spot in this region, but a similar feature is not found in the case of P2-NaM$_{0.10}$NMO. This further supports that there is less oxygen redox in the Mg-doped material. Based on the Ni content in the three compositions, it is also expected that the intensity of the oxygen redox peak for the doped materials should be lower than that of the undoped P2-NaNMO material and also that the doped materials should demonstrate similar intensities for the oxygen redox. In contrast, according to the observed potential profiles and RIXS analysis, we find that the Mg-doped material has the lowest oxygen activity. These results are surprising, because Mg has been a popular element used to trigger oxygen redox in many Mn-based layered oxides such as $Na_{0.67}Mg_{0.28}Mn_{0.72}O_2$[9a, 11] and $Na_{0.67}Mg_{0.33}Mn_{0.67}O_2$,[9a, 11-12] and one would therefore expect Mg doping to enhance the oxygen activity also in Ni/Mn-based layered oxides. The above analysis, however, shows that Mg-doping in Ni-Mn based cathode materials may also suppress the oxygen redox activity. The RIXS data is in line with the electrochemical data, where the Mg-doped sample showed a sloping potential profile in the high voltage region indicating a suppressed oxygen redox activity.

Synchrotron-based *Operando* XRD contour plots for the first charge/discharge cycle are shown in Figure 3 (waterfall XRD plots are shown in Figures S6 and S7). Each material shows a unique structural evolution in the high voltage region, which can be attributed to the influence of the different dopants. It can be observed that the intensity of the main (002) reflection of P2-NaNMO gradually decreased upon charging in the high voltage region, and a new phase appears, as indicated by the appearance of a new reflection at 2.7° (2θ) (see Figure S7 for enlarged view). This phase becomes gradually more dominant and is consistent with the previously reported O2 phase.[5a, 5b, 6c, 9a] Unlike the clear phase change exhibited by P2-NaNMO, the doped materials show more continuous structural evolution in the high voltage region, as can be seen in Figure 3b and c. The main (002) reflection of the Mg-doped material can be seen to gradually shift to higher angles until the OP4 phase is formed in the fully charged state.[6b] The OP4 phase contains layers with alternating octahedral and prismatic stacking of Na in the *c*-axis, leading to the presence of oxygen in four different environments. The OP4 phase can be formed when full slab gliding is prohibited and is related to the reported

"Z-phase" which consists of a continuously evolving intergrowth structure arising from P2 and O2 domains that go through an intermediate OP4 structure.[13] Materials that undergo a P2 to OP4 phase transition will have a much smaller volume change than the P2 to O2 phase transition of the parent material. In the case of P2-$NaS_{0.10}$NMO, no clear phase change is observed in the high voltage region, although there is a change in lattice parameters which indicate a solid solution-type reaction.[14] While the O2 phase of P2-NaNMO and the OP4 phase of P2-$NaM_{0.10}$NMO return to the P2 phase, the structural changes for all samples are not fully reversible, where the lattice parameters are found to not fully recover to their initial state at the beginning of charge.

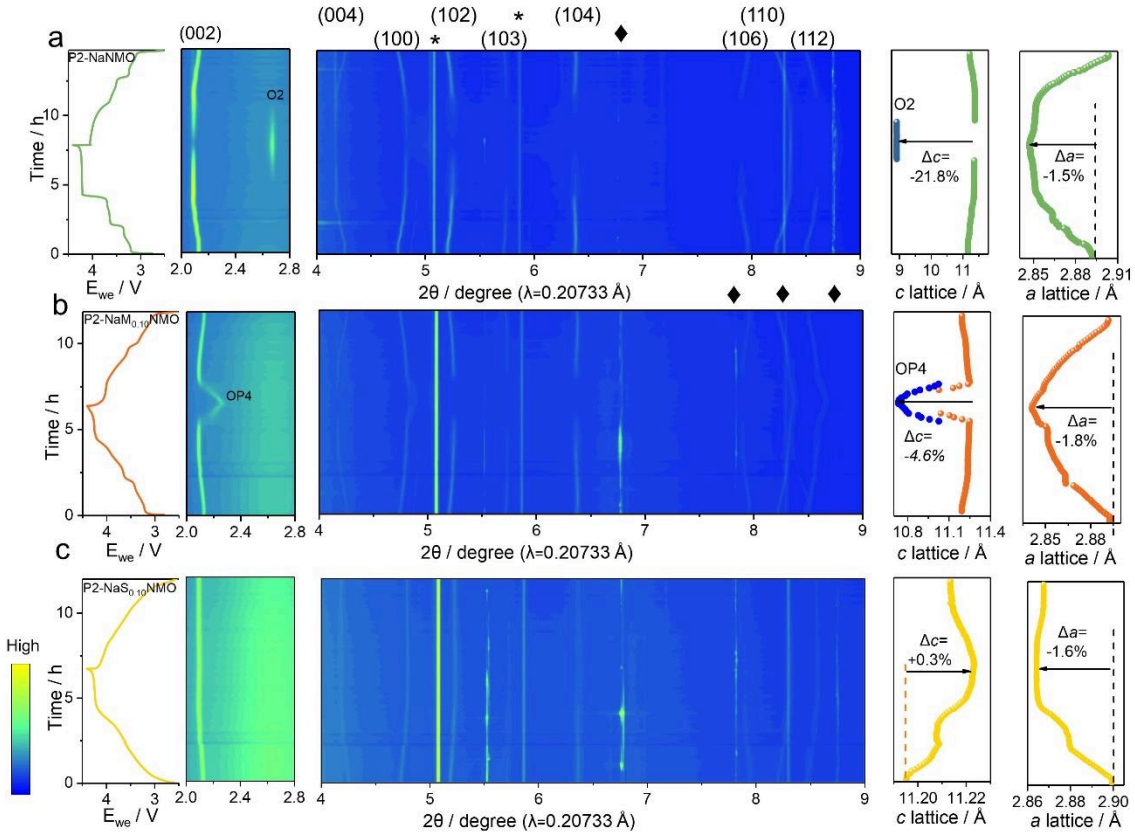

Figure 3 Contour plots of synchrotron-based *operando* XRD measurements during the first charge/discharge process and the corresponding changes in the *c* and *a* lattice parameter for (a) P2-NaNMO, (b) P2-$NaM_{0.10}$NMO and (c) P2-$NaS_{0.10}$NMO. Reflections from the aluminum current collector and sodium metal counter electrode are indicated with * and ♦, respectively.

The corresponding *c* and *a* lattice parameters obtained from the refinement of the XRD patterns are shown next to the contour plots in Figure 3. For all samples, similar trends in the *a* lattice parameter can be observed, with this parameter decreasing during charge and

increasing during discharge, although the reversibility upon discharge differs for each sample. In contrast, all three samples exhibit significant differences in the behavior of the *c* lattice parameter. The *c* lattice parameters in the investigated materials decrease by 21.8% and 4.6% for P2-NaNMO and P2-$NaM_{0.10}$NMO, respectively, while P2-$NaS_{0.10}$NMO demonstrated a 0.3% expansion. Although P2-$NaS_{0.10}$NMO shows the smallest changes in lattice parameters, it also shows the highest structural irreversibility. This is surprising at first because it indicates that it is not the structural changes that dominate cycle life in these materials, but instead the redox behavior is more important. These parameter changes are in line with the observation from pair distribution function (PDF) measurements (see Figure S8). Overall, Mg is found to be the better dopant for $Na_{0.67}Ni_{0.33}Mn_{0.67}O_2$ compared Sc. While Sc-doping is more effective in minimizing the lattice shrinkage during charging, it is less effective in mitigating oxygen redox and shows only a limited structural reversibility during subsequent charging. As a consequence, cycle life is better compared to the parent material but poorer compared to the Mg-doped sample. This shows that the capacity fade is not linked to only volume and structural changes, but instead redox chemistry becomes dominant for dictating cyclability in this case.

X-ray absorption near edge structure (XANES) analysis was used to investigate the changes in oxidation states of Ni and Mn for all samples. Figure 4 (a-c) shows the XANES data for the Ni *K*-edge at different charge/discharge states. When charging to 4.0 V, P2-NaNMO and P2-$NaM_{0.10}$NMO show a small shift towards higher energies relative to the OCV state, whereas P2-$NaS_{0.10}$NMO shows a stronger shift, indicating that more Ni redox is involved in the electrochemical reaction for P2-$NaS_{0.10}$NMO at this stage than in the other compositions. In the high voltage region at 4.4 V, all three samples exhibit distinct energy shifts, indicating that Ni redox also takes place in the high voltage regime. Upon discharge, P2-NaNMO and P2-$NaM_{0.10}$NMO show a high degree of reversibility, almost perfectly overlapping the XAS spectra of the OCV state. For the P2-$NaS_{0.10}$NMO sample, however, the Ni redox is clearly only partially reversible with Ni remaining in a higher oxidation state compared to what was found at OCV, as can be observed by the jump remaining at higher energy for the fully discharged state. This indicates that P2-NaNMO and P2-$NaM_{0.10}$NMO have a better Ni redox reversibility compared to P2-$NaS_{0.10}$NMO in the first cycle, which is consistent with the XRD results. In addition, the Mn *K*-edge XANES at the different charge/discharge states was also collected (see Figure S9 a-c). These results show that Mn is only electrochemically active in the Sc-doped material. In

this case, a $Mn^{3+/4+}$ redox is most probable because the high valence Sc^{3+} replacing the low valence Ni^{2+} requires lowering of the Mn valence for charge compensation. This has the additional consequence of increasing distortion in the MnO_6 octahedra, as evidenced in the comparison of the Mn *K*-edge EXAFS of the samples at OCV in Figure S10d. Here is it shown that despite an overall average octahedral coordination in the samples, the intensity of the Mn-O signal is reduced and shifted slightly to lower radial distances in the case of Sc doping. This suggests greater disorder in the structure which would be consistent with Mn and O existing in multiple sites. This is strongly related to the reported pseudo-Jahn Teller Effect which is known to impact the structural reversibility in Ni-free Mn layered oxides,[15] and can help explain the observed structural irreversibility found during cycling for the Sc-doped material.

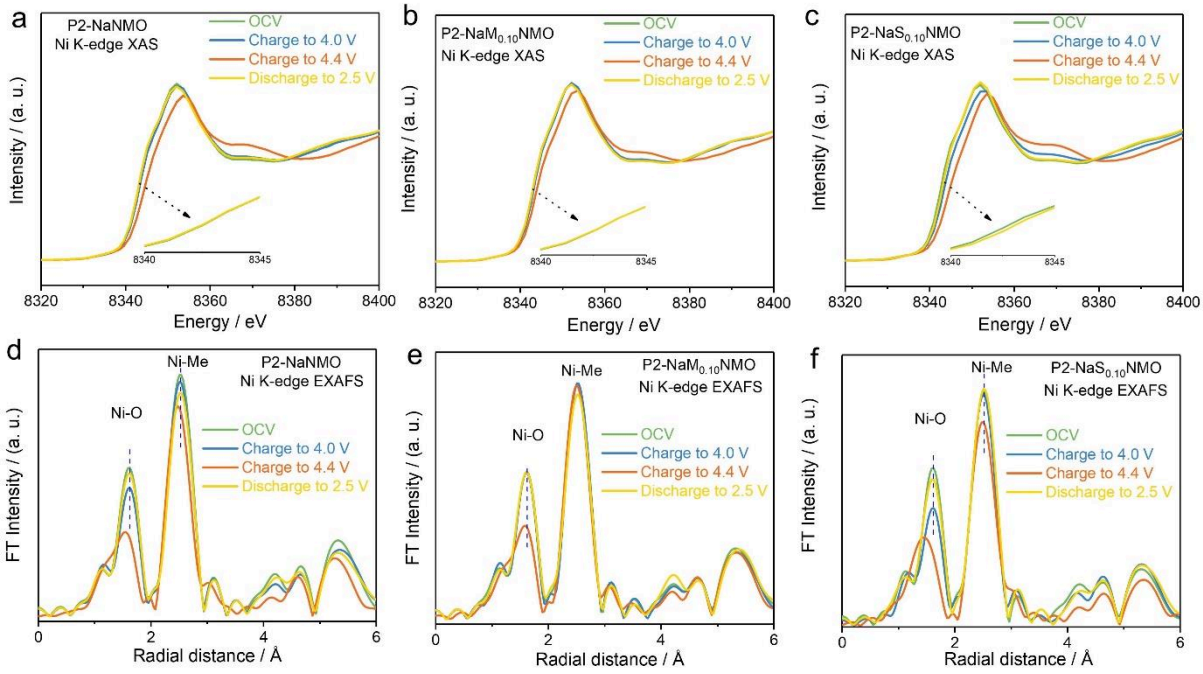

Figure 4 The Ni *K*-edge XANES spectra and corresponding EXAFS spectra at various charge/discharge states for (a, d) P2-NaNMO, (b, e) P2-$NaM_{0.10}$NMO and (c, f) P2-$NaS_{0.10}$NMO. Insets in (a-c) magnify the region between 8340-8345 eV for the OCV and discharge to 2.5 V states in order to highlight the relative irreversibility of P2-$NaS_{0.10}$NMO.

Local structural variations around Ni and Mn were monitored through analysis of the extended X-ray absorption fine structure (EXAFS) at the Ni and Mn *K*-edges (see Figures 4 (d-f) and S10, respectively) for all samples. All of the corresponding EXAFS spectra are characterized by two main features that correspond to the TM-O in the first coordination shell and the TM-Me in

the second coordination shell (where TM is Ni or Mn, and Me is Ni, Mn, or the doping atoms Mg or Sc).[9a, 14b] In Figure 4(d-e), the Fourier transformed (FT) EXAFS spectra at the Ni *K*-edge are shown, where it can be seen that the signal intensities of the Ni-O shell for P2-NaNMO and P2-$NaS_{0.10}$NMO both decrease between the OCV and charged to 4.0 V states, indicating a decrease in coordination number. No change in signal intensity is observed between these two voltages in the case of P2-$NaM_{0.10}$NMO, supporting a higher structure stability in the Mg-doped material. When the voltage is increased to 4.4 V, all materials show a significant reduction in both the radial distance and intensity related to the Ni-O shell, implying that the bond length of Ni-O and the coordination number both decrease. However, the Mn-O bond length in the Mn *K*-edge EXAFS does not appear to change appreciably (see Figure S10c-d).

Combined with the RIXS measurements and the above EXAFS data, it can be concluded that the Ni-O bond length is directly related to the oxygen activity. Based on the *operando* XRD, P2-$NaS_{0.10}$NMO follows a solid solution reaction in the high voltage region. However, the material still shows significant changes in the Ni-O and Ni-Me radial distances and the coordination numbers when charging from 4.0 V to 4.4 V, indicating that the local structural distortion caused by the oxygen redox was much higher. Similar to P2-NaNMO, P2-$NaS_{0.10}$NMO also showed a large decrease in the radial distance and coordination number. However, P2-$NaS_{0.10}$NMO exhibited a larger change in the radial distance compared to the P2-NaNMO material. The P2 to O2 phase transition experienced by the P2-NaNMO material has some small benefits related to limiting the change in radial distance between TM-O, but overall, the phase change is not beneficial due to the global change in lattice parameters. As for P2-$NaM_{0.10}$NMO, it showed the smallest changes among the three samples in the high voltage region due to a less pronounced oxygen redox and moderate phase transition. In the shell of Ni-Me, P2-NaNMO and P2-$NaS_{0.10}$NMO also showed a clear change in the high voltage region, but these changes were quite small, which can be related to the inactive Mn in these compositions. Moreover, the curves for P2-NaNMO and P2-$NaM_{0.10}$NMO in the discharged state can coincide with the OCV state, further demonstrating that the reversibility is higher than that of P2-$NaS_{0.10}$NMO in the first cycle.

In order to understand the above findings, density functional theory (DFT) calculations were used to study the effect of Mg and Sc doping on the lattice parameters and the redox mechanism of P2-$Na_xNi_{0.33}Mn_{0.67}O_2$. The atomic structures of the three materials with Na

contents of x=0.67 and 0.22 (corresponding to the OCV and fully charged states, respectively) were determined (see Figure 5a and Table S5) by performing an extensive set of Coulomb energy and DFT calculations as discussed in the method section. The computed lattice parameters using DFT-PBE+U and DFT-PBE+U+D3 agree with the experimental observations and confirm the oxidation of TMs with desodiation. (For further details, see Table S5 in the Supporting Information).

To characterize the redox mechanism, the magnetic moment (represented by the number of unpaired electrons (N_{unp})) was calculated on the elements and the spin density (SD, Figure. 5b) using DFT-HSE06. The redox mechanism of the elements in each composition was first briefly summarized and compared in Fig. 5b-h and Figure S11. According to our calculated results, the Ni and Mn have the same oxidation state of ~2^+ and ~4^+ for P2-NaNMO and P2-$NaM_{0.10}$NMO in the OCV state (see Figure 5f-h and Figure S11). Upon desodiation from x=0.67 to 0.22, Ni is oxidized to a higher oxidation state and Mn remains almost unchanged. These results are consistent with the XAS results that Ni is the only cation involved in the electrochemical reaction of P2-NaNMO and P2-$NaM_{0.10}$NMO. For the Sc-doped material, the Ni is also ~2^+ in the OCV state, while Mn shows mixed oxidation states of ~3^+ and ~4^+. This is supported by a linear combination analysis of the Mn K-edge XAS data which indicates a significant increase in the presence of Mn 3^+ with Sc doping. As a result, both Ni and Mn are expected to be electrochemically active during the desodiation process which is in line with the XANES measurements. (for further details, please see Figure S11 in the Supporting information).

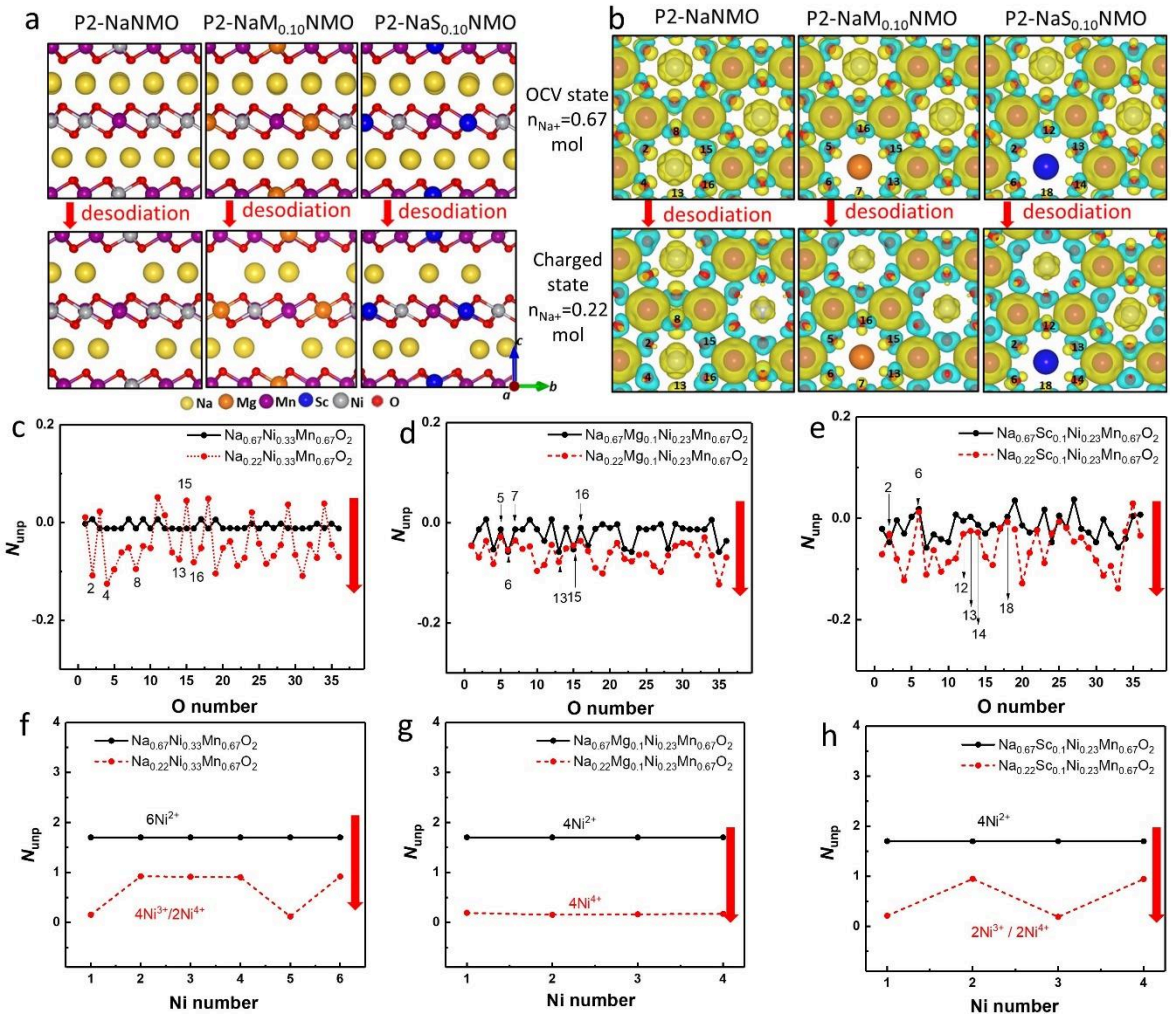

Figure 5 DFT calculations for P2-NaNMO, P2-NaM$_{0.10}$NMO and P2-NaS$_{0.10}$NMO at OCV (n_{Na+}=0.67 mol) and fully charged state (n_{Na+}=0.22 mol). (a) atomistic structures by using DFT-PBE+*U*. (b) Computed spin density plots (an isosurface of 0.006 eV/Å^3) using DFT-HSE06, the up- and down-spin electrons are in yellow and blue, respectively (The atom colors are the same as in (a), but the isosurfaces distort the colors when overlayed). The number of unpaired electrons N_{unp} on O (c-e) and Ni (f-g) for the three materials (black points are for the OCV state and red points are for the fully charged state). The labeled O atoms in (c-e) correspond to the labeled atoms in (b).

In addition to the cation redox**,** oxygen redox was also found in the three materials, in particular for O anions that are close to Ni cations. It can be observed that the calculated value of $\overline{N_{\mathrm{unp}}}$ on O is almost zero for these samples in the OCV states, indicating an average charge of 2− on this anion (see Figure 5c-e and Table S6). Upon desodiation from *x*=0.67 to 0.22, the computed N_{unp} for the O anions show different changes amongst the different materials. For the undoped material, the O anions experience an obvious oxidation during charging, as

shown by the large differences in N_{unp} in the OCV and fully charged states (for example, selected O atoms are highlighted in Figure 5b and their corresponding changes in N_{unp} are highlighted by labeling numbers 2, 4, 8, 13, 15, and 16 in Figure 5c). For the Mg and Sc doped materials, a distinctly different oxidation behavior of the O anions can be observed depending on their nearest neighbor metal ions. O anions that are close to Mg or Sc are inactive, as shown by the very limited change in N_{unp} (see O atoms numbered 5, 6, 7, 13, 15, and 16 for the Mg-doped material in Figure 5b, d and O atoms numbered 2, 6, 12, 13, 14, and 18 in the Sc-doped material in Figure 5c, e). This is in contrast to the oxygen anions surrounding Ni, which show significant changes in N_{unp} for all samples. These differences are greatest in the undoped material, followed by the Sc-doped material, and the Mg-doped material shows the smallest change. This indicates that while all three materials undergo oxygen redox, Mg doping can significantly reduce the oxygen redox activity. These calculations are consistent with the experimental results.

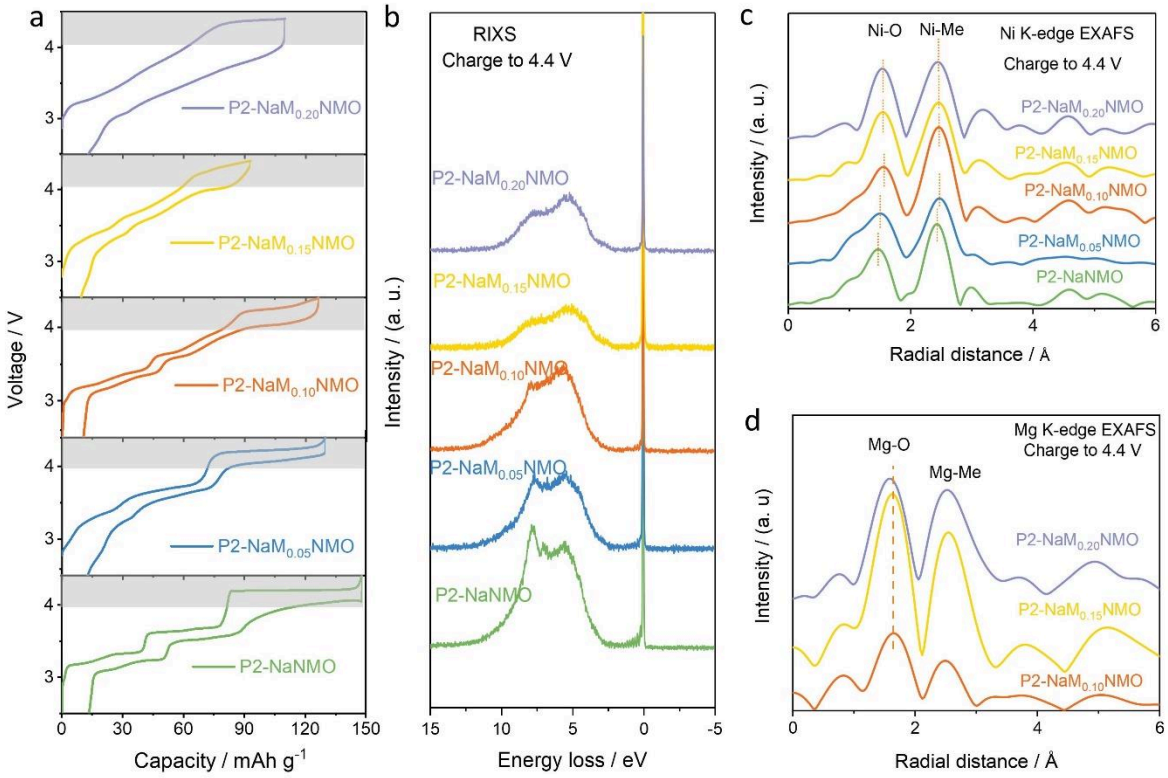

Figure 6 The first charge/discharge curves (a) the RIXS measurement (b) and Ni K-edge EXAFS at the fully charged state (c) for P2-NaNMO, P2-$NaM_{0.5}$NMO, P2-$NaM_{0.10}$NMO, P2-$NaM_{0.15}$NMO, and P2-$NaM_{0.20}$NMO. (d) Mg K-edge EXAFS results at the fully charged state for P2-$NaM_{0.10}$NMO, P2-

$NaM_{0.15}NMO$, and P2-$NaM_{0.20}NMO$. ($Na_{0.67}Ni_xMg_{0.33-x}Mn_{0.67}O_2$, x= 0.05, 0.10, 0.15, and 0.20, designed as P2-$NaM_{0.05}NMO$, P2-$NaM_{0.10}NMO$, P2-$NaM_{0.15}NMO$, and P2-$NaM_{0.20}NMO$)

Mg-doping with varying concentrations (5% - 20%):

The experimental results and the computational study both show that Mg doping (10%) decreases the oxygen activity for P2-$Na_{0.67}Ni_{0.33}Mn_{0.67}O_2$. This can be considered contradictory to other reports on Mn-based layered oxides such as P2-$Na_{0.67}Mg_{0.28}Mn_{0.72}O_2$ that have shown that Mg triggers oxygen redox.[7c, 9a, 11] To further understand the role of Mg in suppressing the oxygen redox activity, a series of materials with different Mg contents (5% to 20%, replacing Ni) were synthesized and investigated by XRD, RIXS, EXAFS, and PDF analysis. The XRD patterns in Figure S12 indicate that all materials have a P2 layered structure with a space group of $P6_3/mmc$, but they exhibit different electrochemical behavior, especially in the high voltage region (grey region in Figure 6a). With increasing Mg-content, the charge/discharge curves become smoother and the corresponding capacity was found to first decrease before increasing again. It was also found that this resulted in increased long-term cycling stability for the 10% Mg-doped sample relative to the other Mg doping concentrations, as shown in Figure S14. The high voltage plateau gradually becomes sloping and then a new flat high voltage plateau reappears as the doping content reaches 20%. The corresponding d*Q*/dV curves in Figure S13 show that the intensity of the peak in the high voltage region also gradually decreases, followed by the appearance of a new and high intensity peak with higher potential. It is worth noting that the same plateau has been reported in literature for the Ni-free compound P2-$Na_{0.67}Mg_{0.28}Mn_{0.72}O_2$, indicating that the oxygen redox may change from Ni-derived to Mg-derived for P2-$NaM_{0.20}NMO$.[9a, 11-12] The results of the RIXS measurements in Figure 6b and Figure S14a are in line with the electrochemical data. The oxygen redox signal at an energy loss of 8 eV gradually decreases, then increases. The P2-$NaM_{0.15}NMO$ sample exhibits the weakest oxygen redox signal, which is consistent with the lowest intensity of the peak in the d*Q*/dV plot (see Figure S13d). The Ni and Mg *K*-edge EXAFS at the fully charged states were also collected and are shown in Figures 6 c and d, respectively. The radial distance of the Ni-O shell increases with Mg doping from P2-NaNMO to P2-$NaM_{0.15}NMO$, and then it shows nearly no change with further increase in the Mg doping content. This indicates that the radial distance of the Ni-O bond length is constant when the Mg doping content is over 15%. Based on the Ni *K*-edge EXAFS results, a shorter Ni-O bond length has a stronger oxygen

redox in $Na_{0.67}Ni_xMg_{0.33-x}Mn_{0.67}O_2$ ($x \leq 0.15$). In the Mg *K*-edge EXAFS, the radial distance of the Mg-O shell shows a similar value for P2-$NaM_{0.10}$NMO and P2-$NaM_{0.15}$NMO, and a smaller value for P2-$NaM_{0.20}$NMO. This result is consistent with what is observed in PDF analysis which probes the global Me-O distances (where Me is Ni, Mn, and/or Mg) and shows that this bond distance increases with Mg doping content from 0 to 15% and then decreases again for P2-$NaM_{0.20}$NMO (see Figure S14b). All of the above results reveal that the Mg-O bond length becomes shortened with increasing Mg doping content, which can therefore activate the oxygen redox in P2-$NaM_{0.20}$NMO. This is also reasonable since the bond length is similarly decreased in P2-$Na_{0.67}Mg_{0.28}Mn_{0.72}O_2$ in the fully charged state.[9a]

Discussion

From the above analysis, we know that both the Ni-O and Mg-O bond lengths will shorten during charging, thereby activating oxygen redox. At the same time, we expect that Ni and Mg share the same lattice sites within the crystal structure, which means that Ni and Mg will surround similar O atoms. Under these circumstances, Ni and Mg in $Na_{0.67}Ni_xMg_{0.33-x}Mn_{0.67}O_2$ will compete for oxygen polarization (Ni-O vs. Mg-O). With no Mg doping (i.e., in the parent P2-NaNMO material), there is nothing to impact the Ni-O bond length, and a 0.06 Å shrinkage of the Ni-O radial distance from the OCV state to the fully charged state can be observed in the Ni EXAFS. As the Mg doping content increases, the O atoms gradually move closer to the Mg atoms, and their distance from the Ni atoms elongates. This corresponds to the observed increase in the Ni-O bond length, and induces the uncommon phenomenon that Mg suppresses the oxygen redox for P2-$Na_{0.67}Ni_{0.33}Mn_{0.67}O_2$. These measurements clarify that the oxygen activity is directly related to the ratio of Mg/Ni, which dictates the degree of oxygen redox for this class of materials.

In this way, we utilize the molar ratio of Mg/Ni in $Na_{0.67}Ni_xMg_{0.33-x}Mn_{0.67}O_2$ ($0 \leq x \leq 0.33$) to clearly demonstrate changes in the oxygen activity, as shown schematically in Figure 8. When the molar ratio of Mg/Ni is close to 1 (P2-$NaM_{0.15}$NMO), the contributions from Ni and Mg towards oxygen polarization become balanced, thereby limiting oxygen redox. When the ratio of Mg/Ni is less than 1 (P2-NaNMO, P2-$NaM_{0.05}$NMO, and P2-$NaM_{0.10}$NMO), the Ni is responsible for triggering oxygen redox, but Mg is able to stabilize the oxygen environment due to its higher covalency and shorter bond length, thereby decreasing the overall oxygen

activity. When the ratio of Mg/Ni is greater than 1 (P2-$NaM_{0.20}NMO$ in this study and P2-$Na_{0.67}Mg_{0.28}Mn_{0.72}O_2$ from the literature[9a, 10]), the Mg becomes responsible for activating oxygen redox, where the Mg-O bond length distortion becomes greater than that of Ni-O. This finding is well supported by DFT results that suggest a higher redox activity of the oxygen for the sample with the highest Mg content ($Na_{0.22}Mg_{0.22}Ni_{0.13}Mn_{0.67}O_2$), see Figure 7a. Due to this competing mechanism, the intensity of the oxygen redox becomes a function of the Mg content with a minimum at P2-$NaMg_{0.15}NMO$, see Figure 7c. Li, Cu, and Zn are also known to trigger oxygen redox in Ni free Mn-based layered oxides, and it is likely that these doping elements have similar concentration-dependent properties to that of Mg in $Na_{0.67}Ni_{0.33}Mn_{0.67}O_2$. P2-$Na_{0.67}(Li, Mg, Zn, Cu)_{0.10}Ni_{0.23}Mn_{0.67}O_2$ samples were prepared with these dopants (10%), as shown in the Supporting Information (Figures S16 and S17), and as predicted, the oxygen redox was also suppressed with the introduction of these dopants (see Figure S18). This demonstrates that the changes in oxygen redox for doping with these elements are also suitable, and we can express this with the equation $Na_{0.67}Ni_x$(Li, Mg, Zn, Cu)$_{0.33-x}Mn_{0.67}O_2$. It is expected that other compositions containing the P2 phase (e.g., with changes in Na concentration) will share these features of inducing a sloping electrochemical behavior when the molar ratio of Ni/Me (Me = Li, Mg, Zn, Cu, or a combination of dopants) is close to 1.

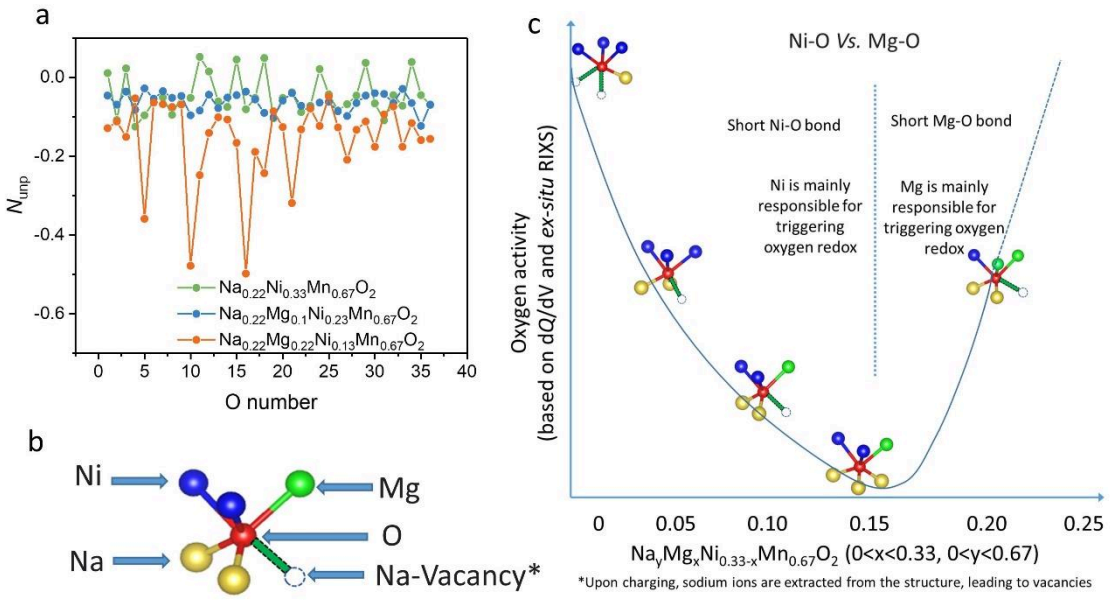

Figure 7(a) DFT calculations of number of unpaired electrons N_{unp} on anions for P2-NaNMO, P2-$NaM_{0.10}NMO$ and P2-$NaMg_{0.22}NMO$ at fully charge state (n_{Na+}=0.22 mol). (b-c) schematic illustration of

a crystal structure and oxygen activity change with the different Mg doping contents in P2-$Na_{0.67}Ni_{0.33}Mn_{0.67}O_2$ at the full charging states, respectively.

Conclusion

In summary, doping with both Mg and Sc significantly improves the cycling stability of $Na_{0.67}Ni_{0.33}Mn_{0.67}O_2$, but two different behaviors are induced in the high voltage region with the different dopants. Table 1 provides a comparison of the electrochemical, structural, and redox behavior observed for the samples with different dopants. While the Sc-doped sample showed the smallest change in lattice parameters, it also presented the highest structural irreversibility during cycling. This demonstrates that it is the redox behavior and not the structural reversibility, as normally understood, that dominates the cycle life in these materials. Through RIXS measurements, we found that both dopants successfully decrease the degree of oxygen redox, but the suppression is strongest in the case of Mg. This result seems to contradict other studies as Mg is well-known to trigger oxygen redox for Ni-free Mn-based layered oxides. In order to determine the origin of the reduced oxygen redox in the Mg-doped materials, a series with different Mg doping concentrations was investigated by RIXS, PDF analysis, and EXAFS. The results demonstrated the presence or disappearance of oxygen redox is dependent on the molar ratio of Mg/Ni in $Na_{0.67}Mg_xNi_{0.33-x}Mn_{0.67}O_2$. When the Mg/Ni ratio was less than (greater than) 1, the Ni (Mg) will play the role of triggering the oxygen redox. A balance is achieved for a Mg/Ni ratio close to 1, where the oxygen redox could be prevented to the greatest degree. This indicates that a balance between Ni-O and Mg-O covalency is the decisive factor for controlling oxygen redox in doped Ni-Mn based layered oxides. This competition is identified as the origin of the lower oxygen activity of P2-$NaM_{0.10}$NMO, which we similarly demonstrated for other dopants that show similar electrochemical behavior in the high voltage region, including Li, Zn, and Cu. Furthermore, it is well-known that oxygen redox is the main bottleneck for cycling life beyond the well-known P2 to O2 phase transition. These findings provide a new direction for understanding the effects of cation doping on the electrochemical behavior of layered oxides.

Table 1 Comparison of the electrochemistry, structure and redox properties among P2-NaNMO, P2-$NaM_{0.10}$NMO and P2-$NaS_{0.10}$NMO.

	Electrochemistry	Structure properties	Redox behavior

	Reversibility of the first cycle	Stability over 500 cycles	Lattice parameter change	Phase transition	Ni (reversibility)	Mn (reversibility)	O (activity)
P2-NaNMO	good	poor	large	P2-O2	high	Not active	high
P2-$NaM_{0.10}NMO$	best	best	intermediate	P2-OP4	high	Not active	lowest
P2-$NaS_{0.10}NMO$	poor	good	least	Solid solution	intermediate	irreversible	low

Experiment details

Synthesis method

A sol-gel method was used to synthesize the precursor followed by high-temperature calcination.[16] $NaNO_3$ (>99.0%, Sigma Aldrich), $Me(CH_3COO)_2$ (Me= Mg, Zn, Cu, CH_3COOLi, >99%, Alfa Aesar), and $Sc(NO_3)_3{\cdot}9H_20$ (>99.99%, abcr Gute Chemie) were dissolved in 80 mL of deionized water in a stoichiometric ratio, mixed for 2 h at 50 ℃ before adding the corresponding amount of citric acid (>99.0%, Sigma Aldrich) (metal: acid=1:1) and mixing for a further 3 h. The temperature was then increased to 120 ℃ to evaporate the water, forming a gel after around 3 h. The gel is then transferred to a crucible and heated in a furnace at 500 ℃ for 5 h. After cooling down to room temperature, the materials were ground to powder, and a pellet was pressed under 15 MPa. The pellets were calcined at 900 ℃ for 10 h and at 950 ℃ for another 10 h in air. The pellets were then transferred to an argon-filled glovebox after the temperature cooled down to 200 ℃.

Electrochemical characterization

The working electrodes were prepared using the active material, Super P (SP, MTI Corp.) and polyvinylidene difluoride (PVDF, MTI Corp) in a weight ratio of 80:10:10. The PVDF binder was dissolved in N-methyl-2-pyrrolidone (NMP, Sigma Aldrich) with a concentration of 0.04 g mL^{-1}. The active material and Super P were mixed in a mortar for 10 min. The PVDF solution was then added, and mixed for another 5 min to form a homogenous slurry, which was then cast onto carbon-coated Al foil (MTI Corp.) with a doctor blade at a thickness of 300 µm. All the above-mentioned steps were carried out in an argon-filled glove box (with H_2O and O_2 concentrations <0.1 ppm). The electrodes were dried on a hot plate and then punched into 12 mm diameter electrodes which were then dried in a Büchi at

120 °C for 12 h. 1 M $NaClO_4$ dissolved in PC:FEC (propylene carbonate, fluoroethylene carbonate, Sigma Aldrich) with a volume ratio of 98:2 was used as the electrolyte and glass fiber (Whatman) as the separator. 2032-type coin cells were assembled in an argon-filled glove box with sodium metal (BASF Corp.) as the counter electrode. All cells were tested in the voltage range between 2.5 and 4.4 V (vs. Na+/Na) using a constant-current protocol at various current densities with a Neware electrochemical workstation (Neware, CT-4008-5V10mA-164).

Structural characterization

Powder XRD was performed with a Bruker D2 Phaser XRD using Cu Kα radiation (λ = 1.5406 Å, 30 kV, 10 mA) between 10° and 70° (2θ) with a step of 0.02°/min. An air-tight Si-based sample holder was used for all measurements. The operando XRD measurements were carried out at beamline P02.1, PETRA- III at DESY (Deutsches Elektronensynchrotron) in Hamburg, Germany, using synchrotron radiation with an energy of ~60 keV (λ=0.20733 Å).[17] The *operando* cells were designed in-house and assembled in an argon-filled glovebox (H_2O and O_2 concentrations <5 ppm, provided by beamline).[18] The electrochemical data were collected using a Biologic VMP-3 potentiostat with an EC-Lab software, which version was 11.34. All the cells were rest for 20 min, then charged/discharged at 0.1 C at a voltage range of 2.5-4.4V. The *operando* XRD data were collected as an ensemble of up to 5 cells simultaneously through the cells with an acquisition time of 1 minute per cell before moving to the next cell using a motorized X-Y stage with a travel range of 350 mm for both directions. The movement of the stages and triggering of the acquisition were controlled by the python3 script. Therefore, for each operando cell a 1-minute measurement was performed every 6 minutes. All the Rietveld refinements of the XRD patterns were performed using GSAS I.

Pair distribution function (PDF) analysis

Total scattering were performed at room temperature using the instrument at beamline P02.1, PETRA III at DESY, Germany. The electrodes were washed with dimethyl carbonate (DMC, Alfa Aesar) and the electrode material was then scraped off the current collector and filled into glass tubes with a diameter of 5 mm. A corner configuration was applied to the all the materials, the acquisition time was set to 6 min, and pdfget3 was used to transform the data.

Resonant inelastic X-ray scattering (RIXS)

RIXS measurements were carried out at room temperature and under 10^{-8} mbar at U41-PEAXIS at BESSY II, Germany.[19] The spectrometer was positioned at specular conditions relative to 60 degree scattering angle and was optimized to a combined resolution of 90 meV using a carbon tape. The excitation energy of each 1D curve was at the O K-edge at 531 eV, and the acquisition time was 20 min.

The excitation energy of each mapping was at the O K-edge at 526 - 534 eV and the acquisition time was 9 h. A vacuum suitcase shown in Figure S19 was used to transfer the sample from an N_2-filled glovebox to the test chamber. The coin cells used for the RIXS measurement were charged/discharged to the target voltage, then disassembled and the electrodes were washed with DMC before drying and spreading onto Cu tape. All steps were carried out in an argon-filled glovebox. Data were processed using the beamline software, Adler-4.0.

Spectroscopic characterization

Ex-situ Ni and Mn K-edge XAS were collected at room temperature at KMC-2 at BESSY II, Germany in both transmission and fluorescence modes.[20] Reference spectra for energy calibration were collected before and after each sample measurement. XAS spectra were obtained by subtracting the pre-edge background from the overall absorption and normalizing to the spline fit using Athena software. The k^2-weighted EXAFS was Fourier transformed over the limited range of k from 3 to 11 $Å^{-1}$. *Ex-situ* Mg K-edge XAS was collected at room temperature in a UHV chamber at PIRX beamline[21] at National Synchrotron Radiation Centre Solaris[22], Poland in the partial (PFY) fluorescence detection mode. The data was processed using Athena software. The k^2-weighted EXAFS was Fourier transformed over the limited range of k from 3 to 8 $Å^{-1}$.

Scanning Electron Microscopy (SEM)

SEM images were taken with a Phenom Pharos Desktop SEM from Phenom world using an accelerating voltage of 10 kV and a secondary electron detector. The corresponding energy-dispersive X-ray spectroscopy (EDX) mapping images also was collected for each sample, and the acquisition time was 20 minutes.

Computational Methods

Spin-polarized DFT calculations were performed using the projector augmented wave (PAW) potential method [23] implemented in the Vienna *Ab Initio* Simulation Package (VASP) code[24]. Generalized gradient approximation (GGA) within the scheme of Perdew–Burke–Ernzerhof (PBE)[25] was used as the basis of the exchange-correlation (*XC*) functional. The Hubbard *U* correction proposed by Dudarev *et al*. [26] with the following *U* values was applied, respectively, for Sc, Mn, and Ni to compute the atomistic structures: 5.0 eV, 5.2 eV, and 6.8. The dispersion D3 correction[27] was added for the low Na concentration. We applied the Heyd–Scuseria–Ernzerhof (HSE06)[28] functional to compute the electronic structure (i.e. number of unpaired electrons (N_{unp}) on elements and spin density). The discharged and charged systems were modeled by 3×3×1 supercells with the following number of atoms: $Na_{12}Ni_6Mn_{12}O_{36}$ (P2-$Na_{0.67}Ni_{0.33}Mn_{0.67}O_2$), $Na_4Ni_6Mn_{12}O_{36}$ (P2-$Na_{0.22}Ni_{0.33}Mn_{0.67}O_2$),

$Na_{12}Mg_2Ni_4Mn_{12}O_{32}$ (P2-$Na_{0.67}Mg_{0.1}Ni_{0.23}Mn_{0.67}O_2$), $Na_4Mg_2Ni_4Mn_{12}O_{36}$ (P2-$Na_{0.22}Mg_{0.1}Ni_{0.23}Mn_{0.67}O_2$), and $Na_{12}Sc_2Ni_4Mn_{12}O_{36}$ (P2-$Na_{0.67}Sc_{0.1}Ni_{0.23}Mn_{0.67}O_2$), $Na_4Sc_2Ni_4Mn_{12}O_{36}$ (P2-$Na_{0.22}Sc_{0.1}Ni_{0.23}Mn_{0.67}O_2$). A Gamma-centered *k*-point mesh of 2×2×2 and an energy cut off of 550 eV as well as an electronic and a force convergence criterion of 10^{-4} eV and $-2.00*10^{-2}$ eV/Å, respectively, were used for DFT calculations. Magnetic moments (number of unpaired electrons) were calculated using a tighter electronic and force convergence criterion of 10^{-6} eV and 10^{-5} eV/Å, respectively. Total Coulomb energy calculations on possible combinations were carried out using the so-called *supercell* code[29]. Atomistic structures and spin density (SD) were visualized with VESTA program[30]. To find the most favorable structures of P2-$Na_{0.67}Ni_{0.33}Mn_{0.67}O_2$ with different *x* values, we modeled and calculated the total Coulomb energy (E_c) of a large number of likely structures. By performing DFT-PBE calculation on the electrostatically most favorable configuration, we determined the lowest total energy structure and used that structure to study charged case as well as Mg and Sc doped system. We used the PBE optimized geometries for further DFT-PBE+*U*, -PBE+*U*+D3 (for $Na_{0.22}$), and -HSE06 calculations. (details please see supporting information)

Acknowledgements

Y. L. thanks the China Scholarship Council for funding. P.A. and K. A. M. thank the Bundesministerium für Bildung und Forschung (BMBF) for funding over project KAROFEST (03XP0498A). P. K. acknowledges the financial support of the German Research Foundation (DFG) with the project number 501562980 as well as the computing time granted through JARA-HPC on the supercomputer JURECA at Forschungszentrum Jülich. We acknowledge DESY (Hamburg, Germany), a member of the Helmholtz Association HGF, for the provision of experimental facilities. Parts of this research were carried out at PETRA III. Beamtime was allocated for proposals I-20220574 and I-20211173. This work was performed using the Biologic VMP-3 potentiostat of DESY/PETRA III beamline P02.1. Y. L. and Y. S acknowledge DESY (Hamburg, Germany), a member of the Helmholtz Association HGF, for the support with travel costs. XAS and RIXS were carried out at the KMC-2 and U41-PEAXIS beamlines, respectively, at the BESSY II electron storage ring operated by the Helmholtz-Zentrum Berlin für Materialien und Energie, GmbH. We thank the Helmholtz-Zentrum Berlin für Materialien und Energie, GmbH for the allocation of synchrotron radiation beamtime. This publication was partly developed under the provision of the Polish Ministry and Higher Education project Support for research and development with the use of research infrastructure of the "National Synchrotron Radiation Centre SOLARIS" under contract nr 1/SOL/2021/2. We acknowledge the SOLARIS Centre for access to the PIRX Beamline, where the measurements were performed.

Conflict of Interest Statement

The authors declare no conflict of interest.

Author Contributions

P.A. and Y. L. conceived the idea, Y. L. synthesized and characterized the materials, performed Rietveld refinement studies, and all electrochemical measurements. *Operando* XRD measurements were done by Y. L., K. A. M., and A. I. F. with the help of V. B. PDF measurements were performed by Y. L. and Y. S. with the help of A. S. J. M. Hard XAS experiments were performed by Y. L., K. A. M., and Y. S. with the help of G. S. Mg *K*-edge XAS was measured by M. Z. and Y. L. RIXS measurements were done by D. W., C. S., and Y. L. DFT was calculated by N. Y. and P. K. The data and manuscript were organized by L.Y. and K. A. M. The manuscript was written by Y. L., K. A. M., and P.A. with contributions from all authors. All authors contributed to discussion of the data analysis.

References

[1] a)P. K. Nayak, L. Yang, W. Brehm, P. Adelhelm, *Angew Chem Int Ed Engl* **2018**, 57, 102; b)R. Usiskin, Y. Lu, J. Popovic, M. Law, P. Balaya, Y.-S. Hu, J. Maier, *Nature Reviews Materials* **2021**, 6, 1020; c)C. Delmas, D. Carlier, M. Guignard, *Advanced Energy Materials* **2020**, 11, 2001201; d)N. Yabuuchi, K. Kubota, M. Dahbi, S. Komaba, *Chem Rev* **2014**, 114, 11636; e)A. Rudola, R. Sayers, C. J. Wright, J. Barker, *Nature Energy* **2023**, 8, 215.

[2] a)C. Ma, J. Alvarado, J. Xu, R. J. Clement, M. Kodur, W. Tong, C. P. Grey, Y. S. Meng, *J Am Chem Soc* **2017**, 139, 4835; b)E. J. Kim, L. A. Ma, L. C. Duda, D. M. Pickup, A. V. Chadwick, R. Younesi, J. T. S. Irvine, A. R. Armstrong, *ACS Applied Energy Materials* **2019**, 3, 184; c)Q. Li, Y. Qiao, S. Guo, K. Jiang, Q. Li, J. Wu, H. Zhou, *Joule* **2018**, 2, 1134; d)C. Cheng, S. Li, T. Liu, Y. Xia, L. Y. Chang, Y. Yan, M. Ding, Y. Hu, J. Wu, J. Guo, L. Zhang, *ACS Appl Mater Interfaces* **2019**, 11, 41304; e)W. Zuo, F. Ren, Q. Li, X. Wu, F. Fang, X. Yu, H. Li, Y. Yang, *Nano Energy* **2020**, 78.

[3] C. Delmas, C. Fouassier, P. Hagenmuller, *Physica B+C* **1980**, 99, 81.

[4] a)R. A. House, U. Maitra, L. Jin, J. G. Lozano, J. W. Somerville, N. H. Rees, A. J. Naylor, L. C. Duda, F. Massel, A. V. Chadwick, S. Ramos, D. M. Pickup, D. E. McNally, X. Lu, T. Schmitt, M. R. Roberts, P. G. Bruce, *Chemistry of Materials* **2019**, 31, 3293; b)W. E. Gent, K. Lim, Y. Liang, Q. Li, T. Barnes, S. J. Ahn, K. H. Stone, M. McIntire, J. Hong, J. H. Song, Y. Li, A. Mehta, S. Ermon, T. Tyliszczak, D. Kilcoyne, D. Vine, J. H. Park, S. K. Doo, M. F. Toney, W. Yang, D. Prendergast, W. C. Chueh, *Nat Commun* **2017**, 8, 2091; c)R. A. House, G. J. Rees, K. McColl, J.-J. Marie, M. Garcia-Fernandez, A. Nag, K.-J. Zhou, S. Cassidy, B. J. Morgan, M. Saiful Islam, P. G. Bruce, *Nature Energy* **2023**, 8, 351; d)D. Eum, B. Kim, J. H. Song, H. Park, H. Y. Jang, S. J. Kim, S. P. Cho, M. H. Lee, J. H. Heo, J. Park, Y. Ko, S. K. Park, J. Kim, K. Oh, D. H. Kim, S. J. Kang, K. Kang, *Nat Mater* **2022**; e)X. Cao, H. Li, Y. Qiao, P. He, Y. Qian, X. Yue, M. Jia, J. Cabana, H. Zhou, *Joule* **2022**, 6, 1290.

[5] a)P. F. Wang, Y. You, Y. X. Yin, Y. S. Wang, L. J. Wan, L. Gu, Y. G. Guo, *Angew Chem Int Ed Engl* **2016**, 55, 7445; b)D. H. Lee, J. Xu, Y. S. Meng, *Phys Chem Chem Phys* **2013**, 15, 3304; c)J. Vergnet, M. Saubanère, M.-L. Doublet, J.-M. Tarascon, *Joule* **2020**, 4, 420.

[6] a)L. Yang, L. Y. Kuo, J. M. López del Amo, P. K. Nayak, K. A. Mazzio, S. Maletti, D. Mikhailova, L. Giebeler, P. Kaghazchi, T. Rojo, P. Adelhelm, *Advanced Functional Materials* **2021**, 31, 2102939; b)G. Singh, N. Tapia-Ruiz, J. M. Lopez del Amo, U. Maitra, J. W. Somerville, A. R. Armstrong, J. Martinez de Ilarduya, T. Rojo, P. G. Bruce, *Chemistry of Materials* **2016**, 28, 5087; c)L. Zheng, J. Li, M. N. Obrovac,

Chemistry of Materials **2017**, 29, 1623; d)X. Wu, G. L. Xu, G. Zhong, Z. Gong, M. J. McDonald, S. Zheng, R. Fu, Z. Chen, K. Amine, Y. Yang, *ACS Appl Mater Interfaces* **2016**, 8, 22227.
[7] a)N. Voronina, M. Y. Shin, H. J. Kim, N. Yaqoob, O. Guillon, S. H. Song, H. Kim, H. D. Lim, H. G. Jung, Y. Kim, H. K. Lee, K. S. Lee, K. Yazawa, K. Gotoh, P. Kaghazchi, S. T. Myung, *Advanced Energy Materials* **2022**; b)B. Peng, Y. Chen, F. Wang, Z. Sun, L. Zhao, X. Zhang, W. Wang, G. Zhang, *Adv Mater* **2022**, 34, e2103210; c)W. Kong, R. Gao, Q. Li, W. Yang, J. Yang, L. Sun, X. Liu, *Journal of Materials Chemistry A* **2019**, 7, 9099.
[8] M. Zhang, D. A. Kitchaev, Z. Lebens-Higgins, J. Vinckeviciute, M. Zuba, P. J. Reeves, C. P. Grey, M. S. Whittingham, L. F. J. Piper, A. Van der Ven, Y. S. Meng, *Nature Reviews Materials* **2022**, 7, 522.
[9] a)E. Boivin, R. A. House, M. A. Pérez-Osorio, J.-J. Marie, U. Maitra, G. J. Rees, P. G. Bruce, *Joule* **2021**, 5, 1267; b)R. A. House, U. Maitra, M. A. Perez-Osorio, J. G. Lozano, L. Jin, J. W. Somerville, L. C. Duda, A. Nag, A. Walters, K. J. Zhou, M. R. Roberts, P. G. Bruce, *Nature* **2020**, 577, 502; c)R. A. House, G. J. Rees, M. A. Pérez-Osorio, J.-J. Marie, E. Boivin, A. W. Robertson, A. Nag, M. Garcia-Fernandez, K.-J. Zhou, P. G. Bruce, *Nature Energy* **2020**, 5, 777.
[10] K. Dai, J. Wu, Z. Zhuo, Q. Li, S. Sallis, J. Mao, G. Ai, C. Sun, Z. Li, W. E. Gent, W. C. Chueh, Y.-d. Chuang, R. Zeng, Z.-x. Shen, F. Pan, S. Yan, L. F. J. Piper, Z. Hussain, G. Liu, W. Yang, *Joule* **2019**, 3, 518.
[11] N. Yabuuchi, R. Hara, K. Kubota, J. Paulsen, S. Kumakura, S. Komaba, *J. Mater. Chem. A* **2014**, 2, 16851.
[12] B. Song, E. Hu, J. Liu, Y. Zhang, X.-Q. Yang, J. Nanda, A. Huq, K. Page, *Journal of Materials Chemistry A* **2019**, 7, 1491.
[13] a)J. W. Somerville, A. Sobkowiak, N. Tapia-Ruiz, J. Billaud, J. G. Lozano, R. A. House, L. C. Gallington, T. Ericsson, L. Häggström, M. R. Roberts, U. Maitra, P. G. Bruce, *Energy & Environmental Science* **2019**, 12, 2223; b)C. Gauckler, M. Dillenz, F. Maroni, L. F. Pfeiffer, J. Biskupek, M. Sotoudeh, Q. Fu, U. Kaiser, S. Dsoke, H. Euchner, P. Axmann, M. Wohlfahrt-Mehrens, A. Groß, M. Marinaro, *ACS Applied Energy Materials* **2022**, 5, 13735.
[14] a)P.-F. Wang, H.-R. Yao, X.-Y. Liu, Y.-X. Yin, J.-N. Zhang, Y. Wen, X. Yu, L. Gu, Y.-G. Guo, *Science Advances* **2018**, 4, eaar6018; b)T. Jin, P. F. Wang, Q. C. Wang, K. Zhu, T. Deng, J. Zhang, W. Zhang, X. Q. Yang, L. Jiao, C. Wang, *Angew Chem Int Ed Engl* **2020**, 2.
[15] J. Zhang, J. B. Kim, J. Zhang, G. H. Lee, M. Chen, V. W. Lau, K. Zhang, S. Lee, C. L. Chen, T. Y. Jeon, Y. W. Kwon, Y. M. Kang, *J Am Chem Soc* **2022**.
[16] L. Yang, J. M. L. Amo, Z. Shadike, S. M. Bak, F. Bonilla, M. Galceran, P. K. Nayak, J. R. Buchheim, X. Q. Yang, T. Rojo, P. Adelhelm, *Advanced Functional Materials* **2020**, 30, 2003364.
[17] a)A.-C. Dippel, H.-P. Liermann, J. T. Delitz, P. Walter, H. Schulte-Schrepping, O. H. Seeck, H. Franz, *Journal of Synchrotron Radiation* **2015**, 22, 675; b)A. Schokel, M. Etter, A. Berghauser, A. Horst, D. Lindackers, T. A. Whittle, S. Schmid, M. Acosta, M. Knapp, H. Ehrenberg, M. Hinterstein, *Journal of Synchrotron Radiation* **2021**, 28, 146.
[18] G. Alvarez Ferrero, G. Åvall, K. A. Mazzio, Y. Son, K. Janßen, S. Risse, P. Adelhelm, *Advanced Energy Materials* **2022**, 12.
[19] C. Schulz, K. Lieutenant, J. Xiao, T. Hofmann, D. Wong, K. Habicht, *Journal of Synchrotron Radiation* **2020**, 27, 238.
[20] D. M. Többens, S. Zander, *Journal of large-scale research facilities JLSRF* **2016**, 2.
[21] M. Zając, T. Giela, K. Freindl, K. Kollbek, J. Korecki, E. Madej, K. Pitala, A. Kozioł-Rachwał, M. Sikora, N. Spiridis, J. Stępień, A. Szkudlarek, M. Ślęzak, T. Ślęzak, D. Wilgocka-Ślęzak, *Nuclear Instruments and Methods in Physics Research Section B: Beam Interactions with Materials and Atoms* **2021**, 492, 43.
[22] J. Szlachetko, J. Szade, E. Beyer, W. Błachucki, P. Ciochoń, P. Dumas, K. Freindl, G. Gazdowicz, S. Glatt, K. Guła, J. Hormes, P. Indyka, A. Klonecka, J. Kołodziej, T. Kołodziej, J. Korecki, P. Korecki, F. Kosiorowski, K. Kosowska, G. Kowalski, M. Kozak, P. Kozioł, W. Kwiatek, D. Liberda, H. Lichtenberg, E. Madej, A. Mandziak, A. Marendziak, K. Matlak, A. Maximenko, P. Nita, N. Olszowska, R. Panaś, E. Partyka-Jankowska, M. Piszak, A. Prange, M. Rawski, M. Roman, M. Rosmus, M. Sikora, J. Sławek, T. Sobol, K. Sowa, N. Spiridis, J. Stępień, M. Szczepanik, M. Ślęzak, T. Ślęzak, T. Tyliszczak, G. Ważny, J.

Wiechecki, D. Wilgocka-Ślęzak, B. Wolanin, P. Wróbel, T. Wróbel, M. Zając, A. Wawrzyniak, M. Stankiewicz, *The European Physical Journal Plus* **2023**, 138.
[23] P. E. Blochl, *Phys Rev B Condens Matter* **1994**, 50, 17953.
[24] G. Kresse, J. Furthmüller, *Physical Review B* **1996**, 54, 11169.
[25] J. P. Perdew, K. Burke, M. Ernzerhof, *Physical Review Letters* **1996**, 77, 3865.
[26] S. L. Dudarev, G. A. Botton, S. Y. Savrasov, C. J. Humphreys, A. P. Sutton, *Physical Review B* **1998**, 57, 1505.
[27] S. Grimme, J. Antony, S. Ehrlich, H. Krieg, *J Chem Phys* **2010**, 132, 154104.
[28] A. V. Krukau, O. A. Vydrov, A. F. Izmaylov, G. E. Scuseria, *J Chem Phys* **2006**, 125, 224106.
[29] K. Okhotnikov, T. Charpentier, S. Cadars, *J Cheminform* **2016**, 8, 17.
[30] K. Momma, F. Izumi, *Journal of Applied Crystallography* **2011**, 44, 1272.

Table of contents

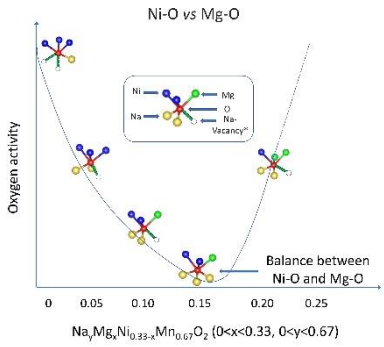

Beyond the well-known P2 to O2 phase transition, oxygen redox is the main bottleneck for capacity retention. Using synchrotron-based methods we reveal that competing mechanisms between Ni and Mg (or Li, Zn, and Cu) are critical for controlling oxygen redox in doped Ni-Mn based layered oxides in Na-ion batteries.